Enhancing performance of low-temperature processed CsPbI₂Br all-inorganic perovskite solar cells using polyethylene oxide-modified TiO₂

Xu Zhao[1),*], *Naitao Gao*[2),*], *Shengcheng Wu*[2)], *Shaozhen Li*[1),✉], *and Sujuan Wu*[2),✉]

1) School of Electrical and Electronic Engineering, Wuhan Polytechnic University, Wuhan 430023, China
2) Institute for Advanced Materials and Guangdong Provincial Key Laboratory of Quantum Engineering and Quantum Materials, South China Academy of Advanced Optoelectronics, South China Normal University, Guangzhou 510006, China

Abstract: CsPbX₃-based (X = I, Br, Cl) inorganic perovskite solar cells (PSCs) prepared by low-temperature process have attracted much attention because of their low cost and excellent thermal stability. However, the high trap state density and serious charge recombination between low-temperature processed TiO₂ film and inorganic perovskite layer interface seriously restrict the performance of all-inorganic PSCs. Here a thin polyethylene oxide (PEO) layer is employed to modify TiO₂ film to passivate traps and promote carrier collection. The impacts of PEO layer on microstructure and photoelectric characteristics of TiO₂ film and related devices are systematically studied. Characterization results suggest that PEO modification can reduce the surface roughness of TiO₂ film, decrease its average surface potential, and passivate trap states. At optimal conditions, the champion efficiency of CsPbI₂Br PSCs with PEO-modified TiO₂ (PEO-PSCs) has been improved to 11.24% from 9.03% of reference PSCs. Moreover, the hysteresis behavior and charge recombination have been suppressed in PEO-PSCs.

Keywords: polyethylene oxide-modified TiO₂ film; low-temperature process; CsPbI₂Br-based all-inorganic perovskite solar cells; photovoltaic performance

1. Introduction

Perovskite solar cells (PSCs) have exhibited a bright future for the next generation of photovoltaic technology due to their low-cost, simple process, and high power conversion efficiency (PCE) [1]. Among them, inorganic cesium lead halide perovskite has attracted great interests because of their good thermal stability [2–3]. Efficiency of all-inorganic PSCs without hole transport layer (HTL) has increased from 2.9% in 2015 to 18.05% in 2023 [4–5]. Although the CsPbI₃ has the most suitable band gap (1.73 eV), it is easy to change from the cubic phase (α-CsPbI₃) to non-photoactive δ-phase due to its high humidity sensitivity [6]. The CsPbBr₃ material reveals high moisture-sustained property, but its band-gap (close to 2.3 eV) is too large as a light-harvesting layer, which will seriously decrease the PCE of devices [7]. Fortunately, CsPbI₂Br material is a good choice among the cesium lead halide perovskites due to its appropriate band gap (1.91 eV) and excellent thermal stability. Although the CsPbI₂Br is a particularly popular perovskite material, the PCE of CsPbI₂Br PSCs is lower than its theoretical limit (over 22%) [6]. Recently, CsPbI₂Br-based PSCs develop rapidly. The CsPbI₂Br-based PSCs with SnO₂/ZnO bilayer electron transport layer (ETL) have achieved a PCE of 14.6% [8]. Thereafter, the PCE of CsPbI₂Br PSCs has been increased to 15.25% by EU(AC)₃ doping into the precursor solution of CsPbI₂Br and 16.42% by using Cs₂CO₃ as interfacial layer at the ZnO/CsPbI₂Br interface, respectively [9–10]. Tang's group [11] has achieved a PCE of 14.14% by inserting a dynamic healing interface in all-inorganic CsPbI₂Br PSCs.

TiO₂ film is usually used as an ETL in PSCs. However, the low conductivity and large oxygen vacancy in low-temperature processed TiO₂ film limit its further development. Modifying or doping TiO₂ film is one of the most popular methods to further enhance the PCE of PSCs based on TiO₂ ETL. Yang's group [12] has used yttrium-doped TiO₂ to promote electron extraction and transfer, but the high trap density caused by oxygen vacancies at the TiO₂/perovskite interface is still unresolved. To solve this problem, some efforts have been tried. It has been found that TiO₂ film modified by RbX (X = Br, I) can prepare high-quality CsPbI₂Br layer on it [13]. Borophene quantum dots can passivate TiO₂ film and form a cascade energy alignment to reduce charge recombination at TiO₂/CsPbI₂Br interface [14]. Wang *et al.* [15] have found that modification of TiO₂ surface by TiCl₄ and TiCl₃ mixture can increase the PCE of carbon-based CsPbI₂Br PSCs. A Sn-doped TiO₂ ETL is used to fabricated an efficient all-inorganic CsPbI₂Br PSC and improve the stability of

*These authors contributed equally to this work.
✉ Corresponding authors: Sujuan Wu   E-mail: sujwu@scnu.edu.cn;   Shaozhen Li   E-mail: origen2003@whpu.edu.cn

Springer

devices [16]. Furthermore, modification of TiO$_2$ film by amorphous antimony sulfide can prepare a multi-contact ETL, resulting in an efficient carbon-based CsPbI$_2$Br PSC with good thermal stability [17].

In fact, the introduction of appropriate organic polymers such as heparin sodium as a passivation layer can also effectively reduce recombination and improve PCE and stability of PSCs [18]. Polyethylene oxide (PEO) buffer layer has been employed to modify CsPbBr$_3$ surface to improve crystallinity and prolong carrier lifetime, leading to enhance PCE and stability of PSCs [19–20]. The mixture of PEO and polyethylene glycol are used as additives to improve the stability of CH$_3$NH$_3$PbI$_3$-based PSCs [21]. Based on above reports, it can be inferred that the PEO can promote the crystallization and improve the stability of perovskite material. Until now, PEO has not been used to optimize the TiO$_2$/CsPbI$_2$Br interface. In order to further passivate trap states and promote carrier transport, low-temperature processed TiO$_2$ ETL has been treated by PEO in this work. On the other hand, even though the PCE of PSCs has been greatly enhanced, organic HTL and evaporated Ag electrode both increase cost and reduce stability of PSCs. To address these issues, CsPbI$_2$Br all-inorganic PSCs are studied.

In this work, the F-doped SnO$_2$ glass (FTO) is used as substrate. All-inorganic planar PSCs with a structure of FTO/TiO$_2$/CsPbI$_2$Br/carbon have been studied. Here, CsPbI$_2$Br perovskite layer is prepared by a low-temperature process and annealed only at 160°C. For the convenience of demonstration, two kinds of CsPbI$_2$Br films/PSCs are investigated: the PEO-film/PSC and reference-film/PSC are related to CsPbI$_2$Br film deposited on TiO$_2$ film with and without PEO modification, respectively. The TiO$_2$/PEO film corresponds to the TiO$_2$ film with PEO modification. The concentrations of PEO solution have been optimized. The champion PCE of PEO-PSC is increased to 11.24% from 9.13% of Reference-PSC at the optimal process. Moreover, PEO-PSCs demonstrate less hysteresis behavior and better stability. The PCE of unsealed PEO-PSC can remain close to 90% of its original value after 20 d stored in air with a (20 ± 5)% humidity at 25°C. The characterizations confirm that PEO passivation layer can effectively reduce defects and non-radiative recombination at TiO$_2$/CsPbI$_2$Br interface and perovskite film to promote charge transfer.

2. Experimental

Polyethylene oxide (PEO, M.W. 100000) was purchased from Alfa Aesar. PEO solutions were prepared by dissolving the PEO in chlorobenzene (CB) solvent with different concentrations and stirred for overnight, respectively. The PEO solution was deposited on TiO$_2$ surface at 4000 r/min for 30 s, then annealed at 100°C for 10 min. The CsPbI$_2$Br precursor solution with 277 mg PbI$_2$, 312 mg CsI, and 220 mg PbBr$_2$ in 1 mL DMSO solvent was spin-coated on TiO$_2$ films at 2500 r/min for 30 s. Next, these films were annealed at 160°C for 10 min. The area of PSCs was 0.095 cm^2. The photo-current of PEO/TiO$_2$ and TiO$_2$ films were gotten from

conductive atomic force microscopy (C-AFM) measurements under 10 mW/cm^2 irradiance with a white LED by an atomic force microscope (AFM) (Asylum Research, Cypher). Elemental distribution (EDS) mapping images were studied by a scanning electron microscopy (SEM, ZEISS ULTRA 55). The photo-voltage (TPV) and photo-current (TPC) decay were recorded by an electrochemical workstation (Zahner, Zennium) in dark. Contact angle was measured by an optical contact angle instrument (Dataphysics OCA Pro 15). All of characterizations were carried out in air. Other experimental materials, fabrication process of TiO$_2$ film and carbon electrode, and characterization methods agree with our reported work [22].

3. Results and discussion

3.1. Microstructure of device and films

Fig. 1 demonstrates structure diagram of PEO-PSC, cross-sectional SEM micrograph of PEO-PSC, and PEO molecular structure. As presented in Fig. 1(b), a clear layer-by-layer structure can be seen in PEO-PSC. According to Fig. S1, average thicknesses of TiO$_2$ and TiO$_2$/CsPbI$_2$Br films are 31 and 339.7 nm, respectively. The PEO layer is too thin to be seen in this scale. As presented in Fig. S1(c), it is about 4.83 nm. Fig. 2(a) and (b) presents SEM micrographs of Reference- and PEO-film. Compared to Reference-film, there are some smaller crystals in PEO-film and their grain boundaries tightly bound together with almost no pinholes on the surface. This phenomenon can be attributed to the fact that PEO polymer film uniformly triggers a heterogeneous nucleation with the perovskite precursor film at the solvent drying stage, resulting in smaller size and more uniform perovskite films [23]. On the other hand, the Fourier transform infrared (FTIR) characterizations confirm the interaction of ETL (or perovskite layer) and PEO in this report, which can help to improve electron transfer from perovskite to cathode for the superior photovoltaic performance of PSCs. This will be discussed in the following. Meanwhile, the inserted contact angles in PEO- and Reference-film are 50.0° and 38.0°, respectively. A larger contact angle in PEO-film is beneficial to improve hydrophobicity and inhibit the water invasion in perovskite film. Fig. 2(c) and (d) demonstrates the SEM images of TiO$_2$ and TiO$_2$/PEO films. The contact angles between TiO$_2$ (or TiO$_2$/PEO) and CB (the solvent of CsPbI$_2$Br precursor solution) are inserted in Fig. 2(c) and (d).
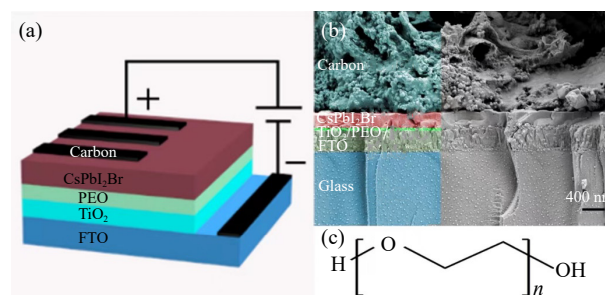

Fig. 1.   (a) Structure diagram of PEO-PSC. (b) Cross-sectional SEM image of PEO-PSC. (c) Molecular structure of PEO.

They are 14.4° and 5.5°, respectively. This result indicates that the TiO$_2$/PEO surface makes the CsPbI$_2$Br precursor solution easier to wet on it, which will help to prepare better CsPbI$_2$Br film [19]. In order to confirm the existence of PEO on TiO$_2$ film, Fig. 2(e)–(h) demonstrates EDS mapping images of TiO$_2$/PEO film. The C element of PEO has been observed, confirming appearance of PEO on TiO$_2$. To further explore the impact of PEO modification on CsPbI$_2$Br layer. Fig. S2 demonstrates X-ray diffraction patterns (XRD) and transmittance spectra of FTO/TiO$_2$ and FTO/TiO$_2$/PEO. Noted that the PEO modification hardly affect the crystallinity and transmittance of TiO$_2$ film. Fig. 2(i) demonstrates XRD of PEO- and Reference-film. The FTO/TiO$_2$ refers to TiO$_2$ film deposited on FTO substrate. Diffraction peaks locating at 14.6° and 29.5° correspond to the (100) and (200)

crystal planes, respectively [7,22]. The diffraction peak position in PEO-film has not changed, indicating that PEO modification has no effect on perovskite crystal structure. The peak intensity in PEO-film is generally stronger than that of Reference-film, confirming that the PEO modification slightly increases the crystallinity of CsPbI$_2$Br film. The PEO concentrations have been optimized by photovoltaic (PV) performance. Fig. S3 demonstrates current density–voltage (J–V) curves and PV parameters of PEO-PSCs as a function of PEO concentrations. Specific PV parameters are presented in Table S1. The PEO-PSCs achieve the best PV performance at the PEO concentration of 0.18 mg/mL. Thus, this is the condition of PEO-PSC/film from Figs. 3 to 8 in all our other experiments.
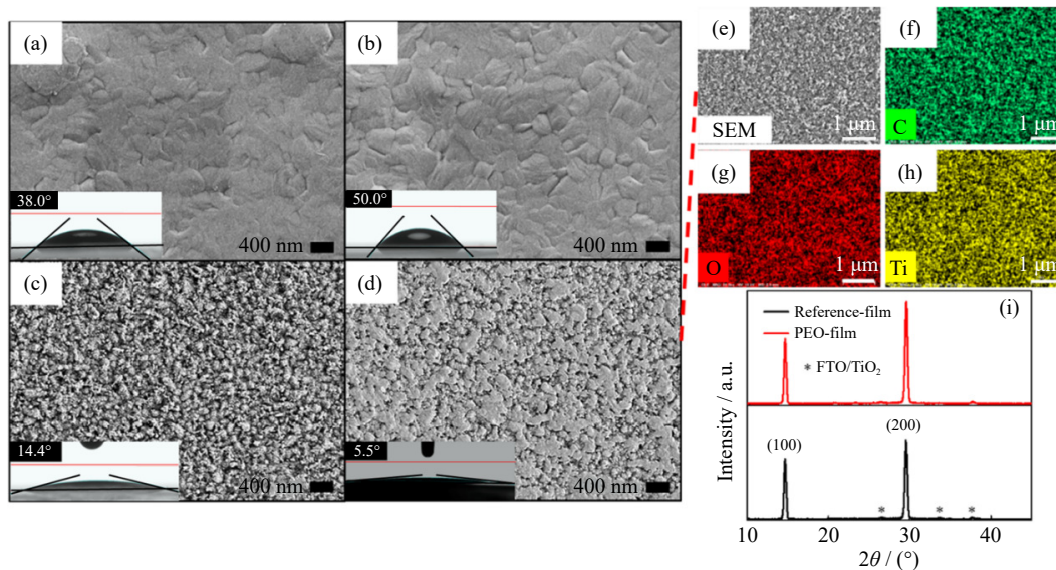

Fig. 2. (a–d) SEM images of Reference-film, PEO-film, TiO$_2$ film, and TiO$_2$/PEO film. (e–h) SEM and corresponding EDS mapping images of TiO$_2$/PEO film. (i) XRD patterns of Reference- and PEO-films. Insets in (a–d) show the photographs of water contact angle for of Reference-film, PEO-film, TiO$_2$ film, and TiO$_2$/PEO film.

3.2. Photovoltaic Performances of PSCs and mechanism study

Fig. 3(a) presents J–V characteristics of PEO- and Reference-PSC measured under reverse (RS) scanning direction. Noted that the PCE, open circuit voltage (V_{oc}), short-circuit current density (J_{sc}), fill factor (FF), and the ratio of parallel resistance to series resistance (R_{sh}/R_s) of PEO-PSCs are larger than those of Reference-PSCs, resulting in an increased champion PCE of 11.24% in PEO-PSCs compared to the 9.13% of Reference-PSCs. Table S2 lists the reported PV parameter statistics about carbon-based CsPbI$_2$Br PSCs. Although the champion PCE of PEO-PSCs is not the best, the PCE of PEO-PSCs has comparability with the reported works. Moreover, our carbon-based HTL-free inorganic PEO-PSCs are prepared by a low-temperature process. In future work, we will try to further improve the PCE by optimizing fabrication process and introducing additives. The FF correlates with R_{sh}/R_s and larger FF in PEO-PSCs can be mainly owed to higher R_{sh}/R_s ratio. Fig. 3(b)–(f) shows the

distributions of PV parameters and R_{sh}/R_s from 35 devices for Reference- and PEO-PSCs. As seen in Fig. 3(b)–(e) and S4, the PV performance of PEO-PSCs has been improved and PV parameters distribute narrower in PEO-PSCs compared to those of Reference-PSCs. Detailed parameters corresponding to Fig. S4 are listed in Tables S3 and S4. The average PCE values for Reference- and PEO-PSCs are 8.70% and 10.89%, respectively. These results confirm that PEO-PSCs have better PV performance and reproductivity [24–25]. To study the impact of PEO modification on hysteresis effect of PSCs, Fig. 4(a) and (b) presents J–V curves of PEO- and Reference-PSC measured under RS and forward (FS) scanning directions. Their specific PV parameters are displayed in Table 1. Hysteresis index (HI) is usually employed to refer hysteresis effect of PSCs using Eq. (1) [26]:

$$HI = \frac{PCE_{RS} - PCE_{FS}}{PCE_{RS}} \qquad (1)$$

where PCE$_{RS}$ and PCE$_{FS}$ refer to the PCE measured in RS and FS scanning directions, respectively. As displayed in Fig. 4(a) and (b) and Table 1, the HI values decrease from 0.220

in Reference-PSC to 0.085 in PEO-PSC. The HI distributions from 35 devices for Reference- and PEO-PSCs are displayed in Figs. 4(c) and S5. Table S5 lists HI values of Reference- and PEO-PSCs from 35 devices each batch. The average HI values for Reference- and PEO-PSCs are 0.214 and

0.081, respectively. Obviously, there is a much lower average HI in PEO-PSCs compare to Reference-PSCs, confirming that hysteresis effects in PEO-PSC have been inhibited. The exact reasons and mechanisms about hysteresis behavior are still a controversial issue. Photo-induced ionic migra-
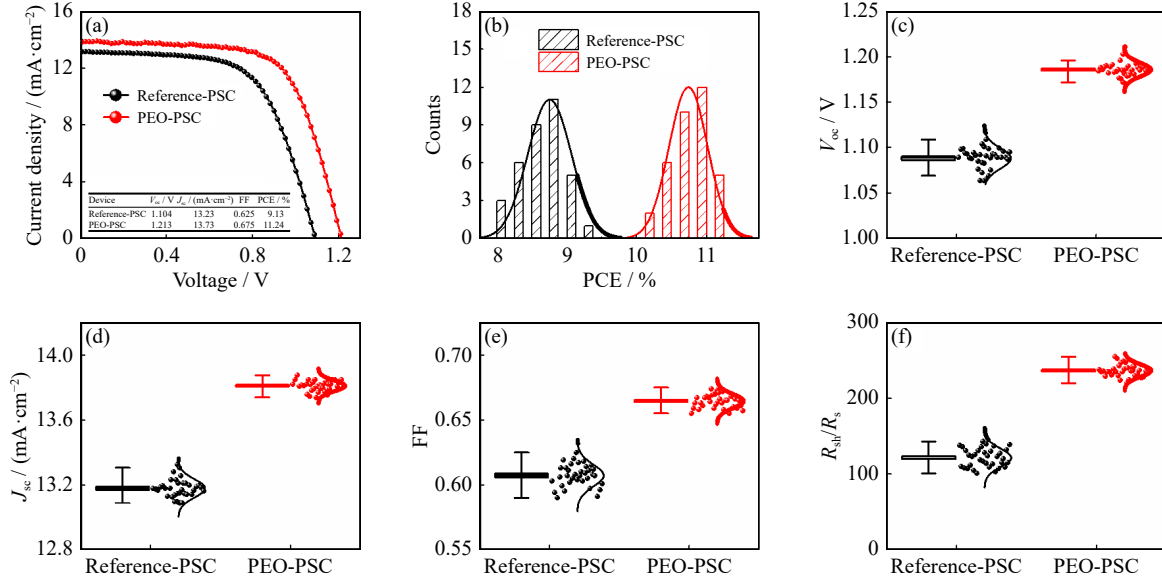

Fig. 3. **(a)** *J–V* **curves of champion devices. (b) Efficiency statistics histograms. (c–f) V_{oc}, J_{sc}, FF, and R_{sh}/R_s distributions of Reference- and PEO-PSCs from 35 devices each batch.**
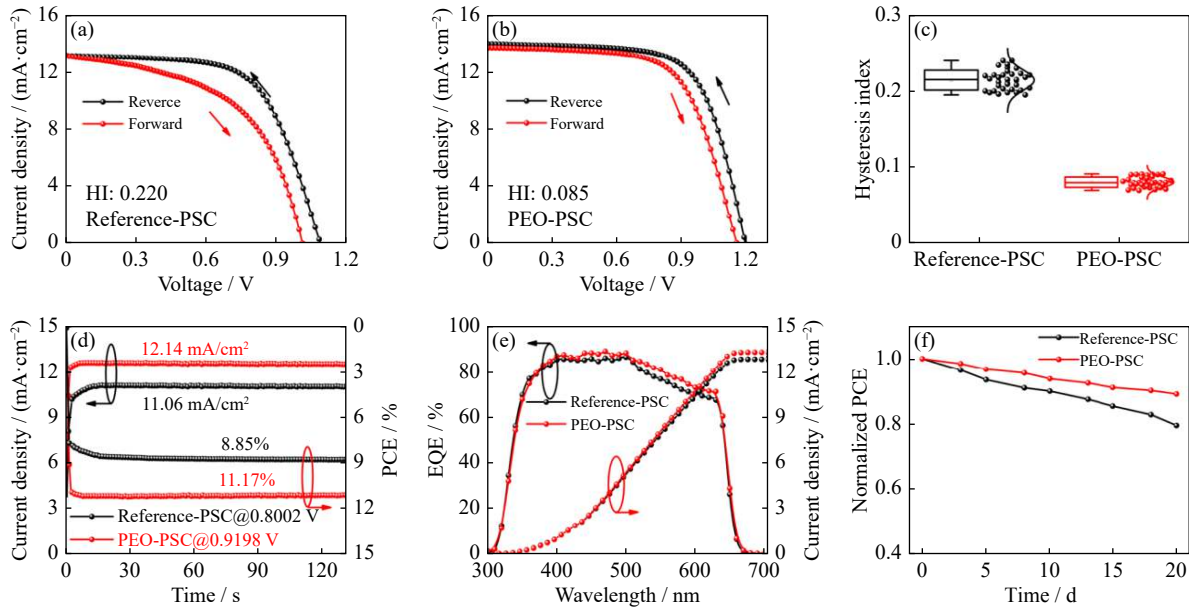

Fig. 4. *J–V* **curves of champion devices characterized under different scanning directions for (a) Reference- and (b) PEO-PSCs. (c) Hysteresis index distributions of PEO- and Reference-PSCs from 35 devices. (d) Steady-state current density and PCE curves of PEO- and Reference-PSCs with a champion PCE. (e) Integrated I_{sc} and EQE curves for PEO- and Reference-PSCs with a champion PCE. (f) Evolution of PCE over days for PEO- and Reference-PSCs.**

Table 1. **PV parameters of Reference- and PEO-PSCs correspond to Fig. 4(a) and (b) characterized under different scanning directions**

Device	Scan direction	V_{oc} / V	J_{sc} / (mA·cm⁻²)	FF	PCE / %	HI
Reference-PSC	RS	1.104	13.23	0.625	9.13	0.212
	FS	1.027	13.09	0.535	7.19	
PEO-PSC	RS	1.213	13.73	0.675	11.24	0.085
	FS	1.156	13.71	0.648	10.28	

tion, charge recombination, ferroelectric properties, and imbalance of electron and hole mobility are possibly the major reasons of PV hysteresis [27–28]. The hysteresis behavior relates to steady-state current density output. The shorter time to reach steady-state, a smaller HI value is [29]. To verify the authenticity of J–V results, their steady-state PCE and current density (I_{sc}) output for PEO-PSCs (@0.9198V) and Reference-PSC (@0.8002V) at their respective voltages and maximum power point with a standard sun have been measured. As displayed in Fig. 4(d), the I_{sc} in PEO-PSCs reaches a stable value faster than that of Reference-PSC. Thus, it takes less time to reach steady-state in PEO-PSCs, which can also indirectly explain the lower HI in PEO-PSCs [30–31]. At the same time, the PCE values of PEO- and Reference-PSC stabilize at 11.17% and 8.85%, respectively. Their I_{sc} values are 12.14 and 11.06 mA/cm^2, respectively. Furthermore, the integrated I_{sc} and external quantum efficiency (EQE) curves of PEO- and Reference-PSC are demonstrated in Fig. 4(e). The respective integrated I_{sc} are 13.26 and 12.86 mA/cm^2, which are very close to their J_{sc} values obtained by the J–V curves (error less than 5%). To investigate the stability of PEO-PSCs, the normalized PCE evolution of unencapsulated Reference- and PEO-PSCs are observed in atmosphere with a $(20 \pm 5)\%$ humidity at 25°C. As demonstrated in Fig. 4(f), the PCE of unsealed PEO-PSC still remains close to 90% (89.1%) of their original values after 20 d, while the PCE of Reference-PSC only remains 79.5% of their original values.

This suggests that the PEO modification can improve the stability of devices.

Fig. 5 displays AFM micrographs of TiO$_2$ and TiO$_2$/PEO films. Root means square (RMS) roughness values for TiO$_2$/PEO and TiO$_2$ are 12.04 and 16.13 nm, respectively. The result confirms that TiO$_2$/PEO film is smoother compared to TiO$_2$ film, which will benefit to improve the contact at TiO$_2$/CsPbI$_2$Br interface. It is known that Kelvin probe atomic force microscopy (KPFM) can map surface potentials on local grains and grain boundaries. Fig. 5(b) and (e) demonstrates KPFM images of TiO$_2$ and TiO$_2$/PEO samples. Obviously, the average contact potential difference (CPD) of TiO$_2$ (511 mV) is higher than that of TiO$_2$/PEO (303 mV). The lower average CPD means that the work function is lower in TiO$_2$/PEO, which is consistent with the reported work [23]. It is reported that the reduced ETL work function can increase the built in potential inside the devices. These will not only increase V_{oc}, but also promote carrier extraction and increase J_{sc} [31–32]. This agree with the increased V_{oc} in PEO-PSCs. Fig. 5(c) and (f) shows C-AFM images and average current of TiO$_2$ and TiO$_2$/PEO film. Obviously, the average current in TiO$_2$/PEO film is higher than that of the TiO$_2$ film. As reported, local current agrees with the local photocurrent characteristics of device [33]. The increased photocurrent in C-AFM measurement confirms the enhanced J_{sc} in PEO-PSCs [32].
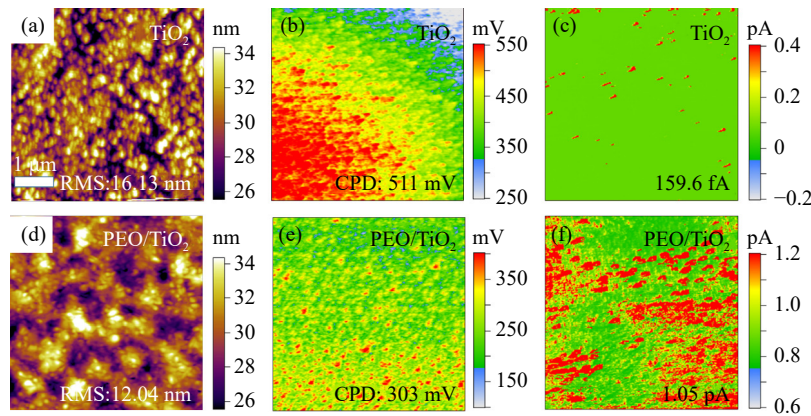

Fig. 5. (a, d) AFM, (b, e) KPFM, and (c, f) C-AFM images of TiO$_2$ and PEO/TiO$_2$ films.

To research the reasons for the increased PCE in PEO-PSC, trap-state density (N_t) of ETL is characterized. The space charge-limited current (SCLC) method is introduced to quantify N_t of ETL [33–34]. Fig. 6 shows the dark current–voltage (I–V) curves and the device structure. As shown in the horizontal coordinate of Fig. 6, the linear region at the low bias voltage corresponds to the ohmic type response. As the bias voltage increases in the middle region, a significant increase in current injection is considered to be the trap-filling process (TFL) [35–36]. The intersection between these two regions is defined as the trap-filling limit voltage (V_{TFL}). The V_{TFL} can be gotten from the I–V measurement, as displayed in Fig. 6. The N_t value can be calculated by the following Eq. (2) [35–36]:

$$N_t = \frac{2\varepsilon\varepsilon_0 V_{TFL}}{qL^2} \tag{2}$$

where q is the element charge (1.6×10^{-19} C); L is the thickness of TiO$_2$/PEO or TiO$_2$ film; the ε and ε_0 are the relative permittivity of ETL (about 50) and vacuum permittivity (about 8.854×10^{-12} F/m), respectively. As presented in Fig. 6, the values of V_{TFL} in TiO$_2$ and TiO$_2$/PEO are 1.313 and 0.803 V, respectively. Therefore, the corresponding N_t values of TiO$_2$ and TiO$_2$/PEO are 7.56×10^{15} and 3.43×10^{15} cm^{-3}, respectively. This indicates that PEO modification can indeed reduce the N_t of TiO$_2$ ETL to promote electron transport and collection [35,37].

Fig. 7(a) presents UV–vis spectra of Reference- and PEO-film. Noted that the PEO modification does not affect the ab-
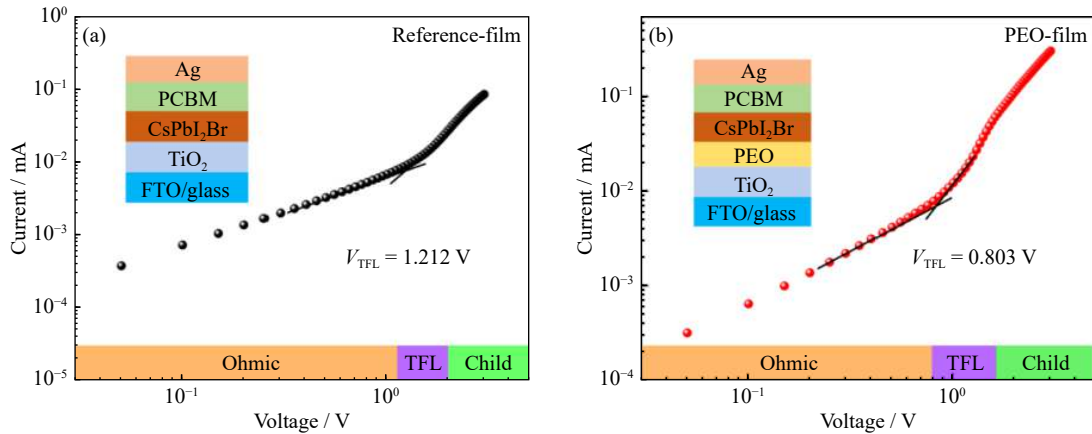
Fig. 6.　Dark *I–V* curves of devices based on (a) reference-film and (b) PEO-film. Inset: corresponding schematic diagram of device structure.

sorbance of CsPbI₂Br perovskite layer. Therefore, the PEO modification hardly influence on the optical absorbance and bandgap of CsPbI₂Br perovskite film [37]. Fig. 7(b) presents steady-state photoluminescence (PL) of PEO- and Reference-film. There is a weaker PL peak intensity in PEO-film than in the Reference-film. As shown in the device structure diagram inserted in Fig. 7(b), the CsPbI₂Br perovskite film are deposited on the FTO/TiO₂ and FTO/TiO₂/PEO substrates, respectively. The intensity of PL peak in PEO-film reduces, suggesting that the PEO modification is more conducive to the transport and extraction of electrons at the inter-

face [37–38]. This result is consistent with *J–V* measurements. Thus, there is a higher electron extraction efficiency in PEO-film than the Reference-film.

The electrochemical impedance spectra (EIS) are often applied to study interface charge transfer and recombination process. Fig. 7(c) demonstrates Nyquist curves of PEO- and Reference-PSC measured under illumination with a bias of −1.1 V. Measured data are fitted by the equivalent-circuit inserted in Nyquist plots. The solid lines and dots correspond to the fitted results and measured data, respectively. Noted that dots and solid lines in Fig. 7(c) coincide well, indicating that
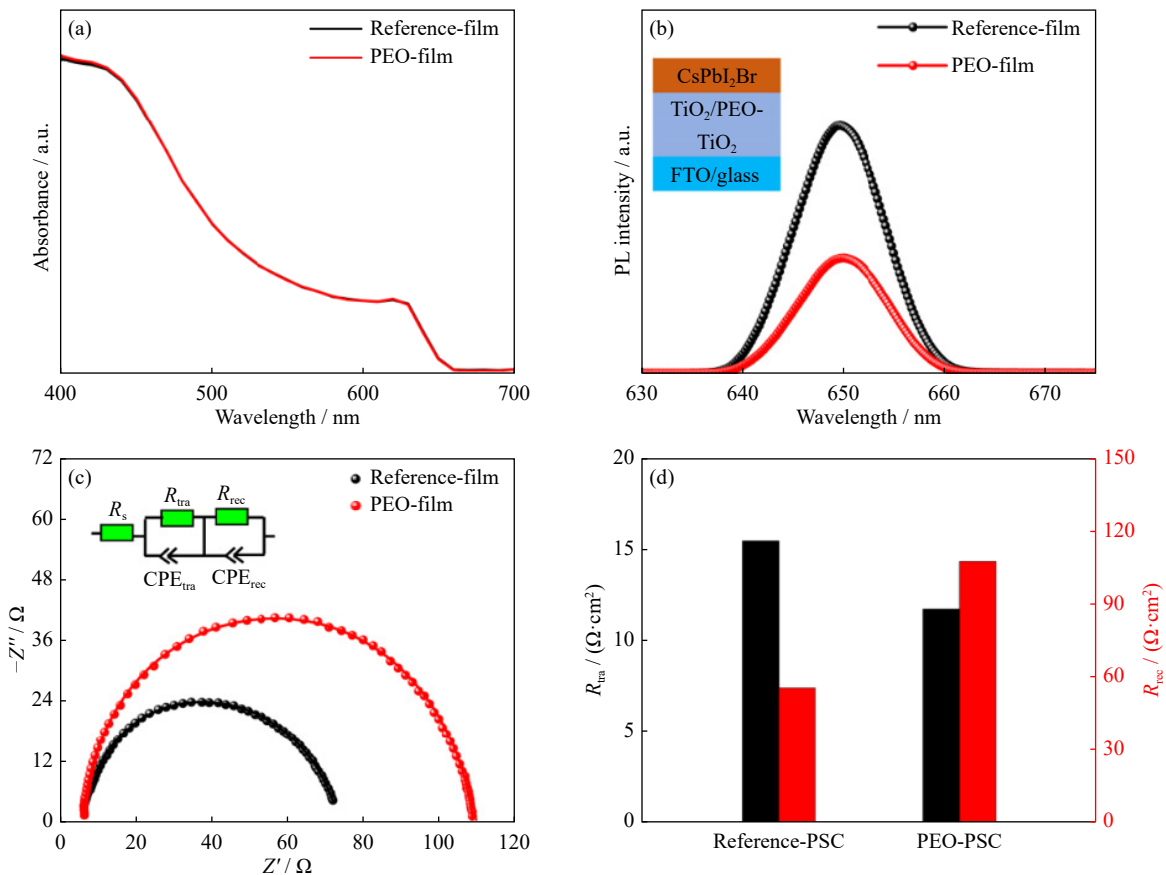

Fig. 7.　(a) UV–vis absorbance spectra of Reference- and PEO-films. (b) Steady-state PL spectra of Reference- and PEO-films deposited on FTO substrate. (c) Nyquist curves. Inset: equivalent circuit diagram employed to fit Nyquist plots. Dots represent measured data and solid lines are the fitting results. (d) Histograms of fitted R_{tra} and R_{rec}.

the fitting circuit is feasible. In the fitted plots, series resistance (R_s) is related to the sheet resistance of FTO substrate and the contact resistance of PSCs, transport resistance (R_{tra}) refers to the transfer resistance at TiO$_2$/perovskite/C interface, and the recombination resistance (R_{rec}) is the composite resistance of device [39–41]. To better fit experimental results, the phase angle element (CPE) is employed to replace original capacitor (C) [42]. The detailed parameters are displayed in Table S6. The similar R_s indicate that the external resistance is homologous in Reference- and PEO-PSC. However, the value of R_{tra} is lower and R_{rec} is larger in PEO-PSC compared to Reference-PSC, as presented in Fig. 7(d). In this work, the perovskite/carbon interface is similar. Thus, the R_{tra} and R_{rec} values correlated with the carrier recombination and transport process at TiO$_2$/CsPbI$_2$Br interface and perovskite film. A lower R_{tra} and a higher R_{rec} in PSCs suggest the promoted charge transport and inhibited carrier recombination in PEO-PSC, which can contribute to obtain better PV performance [43–44]. These confirm that photogenerated electrons can be extracted easier and there is a lower recombination rates at the TiO$_2$/CsPbI$_2$Br interface of PEO-PSC than those of Reference-PSCs.

To further explore charge transport characteristics in the two different PSCs, Fig. 8(a) and (b) displays the TPC and TPV curves. The TPC response decrease from 7.01 μs of Reference-PSC to 5.47 μs of PEO-PSCs, indicating that there is more efficient charge transport in PEO-PSC, which is more

favorable to increase FF and J_{sc} of device [45]. The TPV decay relates to carrier recombination lifetime. As presented in Fig. 8(b), the TPV response time increase from 0.47 ms of Reference-PSC to 0.71 ms of PEO-PSC. The longer lifetime suggests that charge recombination in PEO-PSC is effectively reduced [46–47]. This result confirms that PEO modification can effectively reduce carrier recombination rates at TiO$_2$/CsPbI$_2$Br interface, leading to increasing V_{oc} of PEO-PSC. The curves of V_{oc} and J_{sc} change with the natural logarithms of various light intensities (P_{light}) are tested. The dependence of J_{sc} and V_{oc} on P_{light} follows Eq. (3) [45,48]:

$$J_{sc} \propto P_{light}^{\alpha} \ (\alpha \leq 1) \tag{3}$$

where α is an exponential factor. The α value is nearby 1 in PSCs if space charges do not have impact on it [45,49]. As listed in Fig. 8(c), the α values of PEO- and Reference-PSC are 0.985 and 0.970, respectively. They are all close to 1, suggesting that the bimolecular recombination is negligible in PEO- and Reference-PSC. The following Eq. (4) can be used to study the linear relationship between V_{oc} and P_{light} [45,50–51].

$$V_{oc} = \frac{nkT}{q}\ln(P_{light}) + c \tag{4}$$

where n is the ideal factor, T represent the absolute temperature, k corresponds to the boltzmann constant, and c refer to a constant [45,50–51]. It is reported that the slope is higher than that of kT/q, suggesting that additional trap-assisted re-
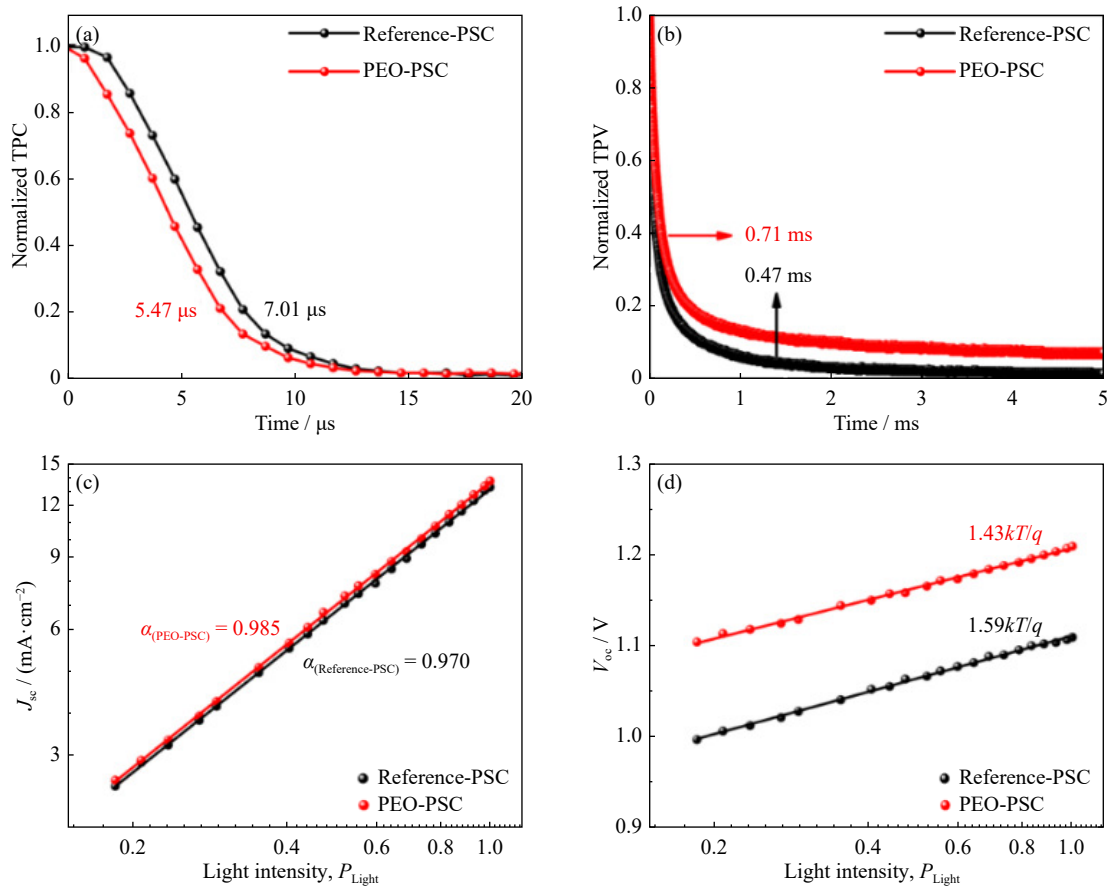

Fig. 8.   **(a, b) TPC and TPV decay curves of Reference- and PEO-PSCs. (c, d) J_{sc} and V_{oc} as a function of light intensity for PEO- and Reference-PSCs.**

combination appears in PSCs [52]. As listed in Fig. 8(d), the slopes of V_{oc} versus P_{light} are $1.59kT/q$ of Reference-PSC and $1.43kT/q$ of PEO-PSC, respectively. Obviously, the slope in PEO-PSC is smaller than that of Reference-PSC. This result means that the energy loss caused by trap-assisted recombination in PEO-PSC is lower, confirming that PEO modification reduces charge recombination at TiO$_2$/CsPbI$_2$Br interface and perovskite film. All these measurements confirm that the PEO modification can decrease charge recombination rates and lead to improving PV performance.

4. Conclusion

In this work, a simple approach is employed to improve the PV performance and stability of low-temperature processed all-inorganic CsPbI$_2$Br PSCs by introducing a facile and efficient interface passivation material PEO to modify the TiO$_2$/CsPbI$_2$Br interface. The PEO modification does not change the morphology and transmittance of TiO$_2$ layer. Moreover, the inserted PEO layer can facilitate electron extraction and inhibit carrier recombination at TiO$_2$/CsPbI$_2$Br interface and perovskite film. At the optimal PEO concentration, PEO-PSCs without encapsulation achieve a champion PCE of 11.24% and steady-state PCE of 11.17% with less hysteresis behavior and better reproducibility, compare to the champion PCE of 9.13% in Reference-PSC. Furthermore, the unsealed PEO-PSCs demonstrate better stability in ambient air than the Reference PSC. This study provides a simple and efficient interfacial engineering method to fabricate efficient, stable, and low-cost PSCs by low-temperature process.

Acknowledgement

Conflict of Interest

All authors declare no conflict of interest.

Supplementary Information

The online version contains supplementary material available at https://doi.org/10.1007/s12613-023-2742-2.

References

[1] L. Chu, S.B. Zhai, W. Ahmad, *et al.*, High-performance large-area perovskite photovoltaic modules, *Nano Res. Energy*, 1(2022), No. 2, art. No. 9120024.

[2] Z.T. Wang, Q.W. Tian, H. Zhang, *et al.*, Managing multiple halide-related defects for efficient and stable inorganic perovskite solar cells, *Angew. Chem. Int. Ed.*, 62(2023), No. 30, art. No. e202305815.

[3] S.Y. Zhang, J. He, X. Guo, *et al.*, Crystallization dynamic control of perovskite films with suppressed phase transition and reduced defects for highly efficient and stable all-inorganic perovskite solar cells, *ACS Mater. Lett.*, 5(2023), No. 6, p. 1497.

[4] G.E. Eperon, G.M. Paternò, R.J. Sutton, *et al.*, Inorganic caesium lead iodide perovskite solar cells, *J. Mater. Chem. A*, 3(2015), No. 39, p. 19688.

[5] J.X. Zhang, G.Z. Zhang, P.Y. Su, *et al.*, 1D choline-PbI$_3$-based heterostructure boosts efficiency and stability of CsPbI$_3$ perovskite solar cells, *Angew. Chem. Int. Ed.*, 62(2023), No. 25, art. No. e202303486.

[6] Q.S. Zeng, X.Y. Zhang, C.M. Liu, *et al.*, Inorganic CsPbI$_2$Br perovskite solar cells: The progress and perspective, *Sol. RRL*, 3(2019), No. 1, art. No. 1800239.

[7] H.P. Dong, Y. Li, S.F. Wang, *et al.*, Interface engineering of perovskite solar cells with PEO for improved performance, *J. Mater. Chem. A*, 3(2015), No. 18, p. 9999.

[8] L. Yan, Q.F. Xue, M.Y. Liu, *et al.*, Interface engineering for all-inorganic CsPbI$_2$Br perovskite solar cells with efficiency over 14%, *Adv. Mater.*, 30(2018), No. 33, art. No. 1802509.

[9] S.M. Yang, H. Zhao, Y. Han, C.Y. Duan, Z.K. Liu, and S.F. Liu, Europium and acetate co-doping strategy for developing stable and efficient CsPbI$_2$Br perovskite solar cells, *Small*, 15(2019), No. 46, art. No. 1904387.

[10] E.C. Shen, J.D. Chen, Y. Tian, *et al.*, Interfacial energy level tuning for efficient and thermostable CsPbI$_2$Br perovskite solar cells, *Adv. Sci.*, 7(2020), No. 1, art. No. 1901952.

[11] Q.Y. Guo, J.L. Duan, J.S. Zhang, *et al.*, Universal dynamic liquid interface for healing perovskite solar cells, *Adv. Mater.*, 34(2022), No. 26, art. No. 2202301.

[12] H.P. Zhou, Q. Chen, G. Li, *et al.*, Interface engineering of highly efficient perovskite solar cells, *Science*, 345(2014), No. 6196, p. 542.

[13] J.J. He, B. Ge, Y. Hou, S. Yang, and H.G. Yang, A dendrite-structured RbX (X=Br, I) interlayer for CsPbI$_2$Br perovskite solar cells with over 15 % stabilized efficiency, *ChemSusChem*, 13(2020), No. 20, p. 5443.

[14] A.R. Zhao, Y. Han, Y.H. Che, *et al.*, High-quality borophene quantum dot realization and their application in a photovoltaic device, *J. Mater. Chem. A*, 9(2021), No. 42, p. 24036.

[15] W.R. Wang, Y. Lin, G.Z. Zhang, *et al.*, Modification of compact TiO$_2$ layer by TiCl$_4$–TiCl$_3$ mixture treatment and construction of high-efficiency carbon-based CsPbI$_2$Br perovskite solar cells, *J. Energy Chem.*, 63(2021), p. 442.

[16] C.H. Duan, Q.Y. Wen, Y. Fan, J. Li, Z.D. Liu, and K.Y. Yan, Improving the stability and scalability of all-inorganic inverted CsPbI$_2$Br perovskite solar cell, *J. Energy Chem.*, 68(2022), p. 176.

[17] Y. Jing, X. Liu, Y. Xu, *et al.*, Amorphous antimony sulfide nanoparticles construct multi-contact electron transport layers for efficient carbon-based all-inorganic CsPbI$_2$Br perovskite solar cells, *Chem. Eng. J.*, 455(2023), art. No. 140871.

[18] S. You, H. Wang, S.Q. Bi, *et al.*, A biopolymer heparin sodium interlayer anchoring TiO$_2$ and MAPbI$_3$ enhances trap passivation and device stability in perovskite solar cells, *Adv. Mater.*, 30(2018), No. 22, art. No. 1706924.

[19] J. Tan, J. Dou, J.L. Duan, Y.Y. Zhao, B.L. He, and Q.W. Tang, A trifunctional polyethylene oxide buffer layer for stable and efficient all-inorganic CsPbBr$_3$ perovskite solar cells, *Dalton Trans.*, 52(2023), No. 13, p. 4038.

[20] K. Tian, Y. Lu, R. Liu, X.J. Loh, and D.J. Young, Low-threshold amplified spontaneous emission from air-stable CsPbBr$_3$ perovskite films containing trace amounts of polyethylene oxide, *ChemPlusChem*, 86(2021), No. 11, p. 1537.

[21] Z. Uddin, J.H. Ran, E. Stathatos, and B. Yang, Improving thermal stability of perovskite solar cells by thermoplastic additive engineering, *Energies*, 16(2023), No. 9, art. No. 3621.

[22] J.J. Yang, X. Yu, X.B. Lu, *et al.*, Bifunctional passivation for efficient and stable low-temperature processed all-inorganic CsPbIBr$_2$ perovskite solar cells, *Surf. Interfaces*, 32(2022), art.

No. 102097.

[23] P.L. Qin, T. Wu, Z.C. Wang, *et al*., Vitrification transformation of poly(ethylene oxide) activating interface passivation for high-efficiency perovskite solar cells, *Sol. RRL*, 3(2019), No. 10, art. No. 1900134.

[24] N. Arora, M.I. Dar, A. Hinderhofer, *et al*., Perovskite solar cells with CuSCN hole extraction layers yield stabilized efficiencies greater than 20%, *Science*, 358(2017), No. 6364, p. 768.

[25] Q. Chen, H.P. Zhou, Z.R. Hong, *et al*., Planar heterojunction perovskite solar cells via vapor-assisted solution process, *J. Am. Chem. Soc.*, 136(2014), No. 2, p. 622.

[26] B.A. Nejand, V. Ahmadi, S. Gharibzadeh, and H.R. Shahverdi, Cuprous oxide as a potential low-cost hole-transport material for stable perovskite solar cells, *ChemSusChem*, 9(2016), No. 3, p. 302.

[27] A. Aftab and M.I. Ahmad, A review of stability and progress in tin halide perovskite solar cell, *Sol. Energy*, 216(2021), p. 26.

[28] H.J. Snaith, A. Abate, J.M. Ball, *et al*., Anomalous hysteresis in perovskite solar cells, *J. Phys. Chem. Lett.*, 5(2014), No. 9, p. 1511.

[29] J.Y. Li, B.Y. Huang, E.N. Esfahani, *et al*., Touching is believing: Interrogating halide perovskite solar cells at the nanoscale via scanning probe microscopy, *NPJ Quantum Mater.*, 2(2017), art. No. 56.

[30] B.P. Nguyen, G.Y. Kim, W. Jo, B.J. Kim, and H.S. Jung, Trapping charges at grain boundaries and degradation of $CH_3NH_3Pb(I_{1-x}Br_x)_3$ perovskite solar cells, *Nanotechnology*, 28(2017), No. 31, art. No. 315402.

[31] J.H. Heo, M.S. You, M.H. Chang, *et al*., Hysteresis-less mesoscopic $CH_3NH_3PbI_3$ perovskite hybrid solar cells by introduction of Li-treated TiO_2 electrode, *Nano Energy*, 15(2015), p. 530.

[32] K.M. Boopathi, R. Mohan, T.Y. Huang, *et al*., Synergistic improvements in stability and performance of lead iodide perovskite solar cells incorporating salt additives, *J. Mater. Chem. A*, 4(2016), No. 5, p. 1591.

[33] Y.F. Liu, Z.L. Wu, Y.X. Dou, *et al*., Formamidinium-based perovskite solar cells with enhanced moisture stability and performance via confined pressure annealing, *J. Phys. Chem. C*, 124(2020), No. 23, p. 12249.

[34] Y. Dong, W.J. Shen, W. Dong, *et al*., Chlorobenzenesulfonic potassium salts as the efficient multifunctional passivator for the buried interface in regular perovskite solar cells, *Adv. Energy Mater.*, 12(2022), No. 20, art. No. 2200417.

[35] Y.X. Gao, Y.N. Dong, K.Q. Huang, *et al*., Highly efficient, solution-processed CsPbI$_2$Br planar heterojunction perovskite solar cells via flash annealing, *ACS Photonics*, 5(2018), No. 10, p. 4104.

[36] J.R. Zhang, D.L. Bai, Z.W. Jin, *et al*., 3D–2D–0D interface profiling for record efficiency all-inorganic CsPbBrI$_2$ perovskite solar cells with superior stability, *Adv. Energy Mater.*, 8(2018), No. 15, art. No. 1703246.

[37] Y. Xu, F.L. Liu, R.S. Li, *et al*., Mxene regulates the stress of perovskite and improves interface contact for high-efficiency

[38] Y.W. Duan, K. He, L. Yang, J. Xu, W.J. Zhao, and Z.K. Liu, 24.20%-efficiency MA-free perovskite solar cells enabled by siloxane derivative interface engineering, *Small*, 18(2022), No. 48, art. No. 2204733.

[39] Y.X. Zhao, A.M. Nardes, and K. Zhu, Mesoporous perovskite solar cells: Material composition, charge-carrier dynamics, and device characteristics, *Faraday Discuss.*, 176(2014), p. 301.

[40] M. Park, J.Y. Kim, H.J. Son, C.H. Lee, S.S. Jang, and M.J. Ko, Low-temperature solution-processed Li-doped SnO$_2$ as an effective electron transporting layer for high-performance flexible and wearable perovskite solar cells, *Nano Energy*, 26(2016), p. 208.

[41] Z.H. Yu, B.L. Chen, P. Liu, *et al*., Stable organic–inorganic perovskite solar cells without hole-conductor layer achieved via cell structure design and contact engineering, *Adv. Funct. Mater.*, 26(2016), No. 27, p. 4866.

[42] L.Y. Lin, M.H. Yeh, C.P. Lee, C.Y. Chou, R. Vittal, and K.C. Ho, Enhanced performance of a flexible dye-sensitized solar cell with a composite semiconductor film of ZnO nanorods and ZnO nanoparticles, *Electrochim. Acta*, 62(2012), p. 341.

[43] S. Yang, W.B. Yue, J. Zhu, Y. Ren, and X.J. Yang, Graphene-based mesoporous SnO$_2$ with enhanced electrochemical performance for lithium-ion batteries, *Adv. Funct. Mater.*, 23(2013), No. 28, p. 3570.

[44] M.A. Mahmud, N.K. Elumalai, M.B. Upama, *et al*., Single vs mixed organic cation for low temperature processed perovskite solar cells, *Electrochim. Acta*, 222(2016), p. 1510.

[45] X.M. Li, P.C. Jia, F.W. Meng, *et al*., Propylamine hydrobromide passivated tin-based perovskites to efficient solar cells, *Int. J. Miner. Metall. Mater.*, 30(2023), No. 10, p. 1965.

[46] H.R. Sun, J. Zhang, X.L. Gan, *et al*., Pb-reduced CsPb$_{0.9}$Zn$_{0.1}$I$_2$Br thin films for efficient perovskite solar cells, *Adv. Energy Mater.*, 9(2019), No. 25, art. No. 1900896.

[47] W. Chen, Y.H. Wu, J. Fan, *et al*., Understanding the doping effect on NiO: Toward high-performance inverted perovskite solar cells, *Adv. Energy Mater.*, 8(2018), 19, art. No. 1703519.

[48] J.J. Tian, Q.F. Xue, X.F. Tang, *et al*., Dual interfacial design for efficient CsPbI$_2$Br perovskite solar cells with improved photostability, *Adv. Mater.*, 31(2019), No. 23, art. No. 1901152.

[49] R. Azmi, S.H. Oh, and S.Y. Jang, High-efficiency colloidal quantum dot photovoltaic devices using chemically modified heterojunctions, *ACS Energy Lett.*, 1(2016), No. 1, p. 100.

[50] Y. Zhou, X. Zhang, X.B. Lu, *et al*., Promoting the hole extraction with Co$_3$O$_4$ nanomaterials for efficient carbon-based CsPbI$_2$Br perovskite solar cells, *Sol. RRL*, 3(2019), No. 4, art. No. 1800315.

[51] J.L. Duan, Y.Y. Zhao, B.L. He, and Q.W. Tang, High-purity inorganic perovskite films for solar cells with 9.72 % efficiency, *Angew. Chem. Int. Ed.*, 57(2018), No. 14, p. 3787.

[52] M. Zhang, W. Gao, F.J. Zhang, *et al*., Efficient ternary nonfullerene polymer solar cells with PCE of 11.92% and FF of 76.5%, *Energy Environ. Sci.*, 11(2018), No. 4, p. 841.